A Localized Quantitative Precipitation Estimation for S-Band Polarimetric Radar in Taiwan

YU-SHUANG TANG,[a,b] PAO-LIANG CHANG,[a] WEI-YU CHANG,[b] JIAN ZHANG,[c] LIN TANG,[d] PIN-FANG LIN,[a]
AND CHIA-RONG CHEN[a]

[a] *Central Weather Administration, Taipei, Taiwan*
[b] *National Central University, Taoyuan City, Taiwan*
[c] *NOAA/OAR/National Severe Storms Laboratory, Norman, Oklahoma*
[d] *Cooperative Institute for Severe and High-Impact Weather Research and Operations, Norman, Oklahoma*

(Manuscript received 20 November 2023, in final form 20 July 2024, accepted 20 August 2024)

ABSTRACT: A polarimetric radar quantitative precipitation estimation (QPE) to estimate the rain rate R from specific attenuation A has been applied in Taiwan's operational Quantitative Precipitation Estimation and Segregation Using Multiple Sensors (QPESUMS) system since 2016. A 3-yr (2016–18) drop size distribution (DSD) dataset from an operational Particle Size and Velocity (Parsivel) network was used to derive a localized coefficient as well as the $\alpha(K)$ function in the $R(A)$ scheme for S-band radar, where α is a key parameter in the estimation of A and K is the linear fitted slope of differential reflectivity Z_{DR} versus reflectivity Z. The local drop size distribution data were also used to derive the localized $R(Z)$ and $R(K_{\mathrm{DP}})$ relationships, and the relationships were evaluated using radar observations in heavy rain cases. A synthetic quantitative precipitation estimate combining the localized $R(A)$, $R(Z)$, and $R(K_{\mathrm{DP}})$ relationships is compared to its operational counterpart and showed about 8% reduction in the normalized mean error for the mei-yu cases. Typhoon cases exhibited similar improvements by the localized QPE relationships but showed higher uncertainties than in the mei-yu cases. The higher uncertainties in the typhoon QPE verification were likely due to the stronger winds in typhoons than in the mei-yu events that caused greater mismatches between the radar observations at an altitude and the gauges at the ground. Overall, the results demonstrated advantages of localized radar rainfall relationships derived from the disdrometer data to improve the accuracy of the operational rainfall estimation products.

SIGNIFICANCE STATEMENT: A 3-yr (2016–18) drop size distribution (DSD) dataset from the operational Parsivel network in Taiwan was utilized to localize parameters in the QPE relationships for S-band dual-polarimetric radar. These relationships were evaluated using radar observations in the mei-yu front and typhoon events in Taiwan. The results show that using localized radar rainfall relationships derived from the disdrometer data can enhance the accuracy of the operational rainfall products.

KEYWORDS: Precipitation; Drop size distribution; Radars/Radar observations

1. Introduction

Taiwan is a mountainous island situated in the western Pacific Ocean that is primarily characterized by the Central Mountain Range (CMR), which spans most of Taiwan in a north-northeast to south-southwest direction. To improve the monitoring and prediction of flash floods, debris flows, and severe storms over the complex terrain of Taiwan, a radar network was installed in 2002 (Chang et al. 2021), which has been continuously enhanced and upgraded. As of September 2023, the network consists of four S-band and six C-band dual-polarization radars. With the dense radar network, an operational radar data integration system called Quantitative Precipitation Estimation and Segregation Using Multiple Sensors (QPESUMS) was developed and a suite of high-resolution (1 km, 10 min) quantitative precipitation estimate (QPE) and severe weather products are generated to support the Central Weather Administration (CWA) operations and many other government agencies in Taiwan. The operational radar QPE product was based on a synthetic technique merging precipitation rates derived from $R(Z)$, $R(A)$, and $R(K_{\mathrm{DP}})$ relationships (Chang et al. 2021).

Before polarimetric weather radars become available for operations, Z–R relationships [hereafter "$R(Z)$"] are widely used to calculate the QPE. Previous studies showed that the $R(Z)$ relations are sensitive to drop size distributions (DSDs) affected by precipitation types and geographical regions (Fulton et al. 1998; Marshall et al. 1955; Xin et al. 1997; Chen et al. 2021). Further, attenuation, wet radome, partial beam blockage, etc., can significantly affect the reflectivity data quality, causing large uncertainties in the $R(Z)$-based QPE.

Polarimetric radar can observe several variables in addition to Z, which include differential reflectivity (Z_{DR}, dB), differential phase (Φ_{DP}, °), specific differential phase (K_{DP}, ° km^{-1}), and correlation coefficient (ρ_{HV}). Seliga et al. (1981) indicated that using Z and Z_{DR} can reduce the effect of DSD variability in the radar QPE. The Z_{DR} is helpful to reveal the DSD variability in different weather systems (Zrnić and Ryzhkov 1999).

Denotes content that is immediately available upon publication as open access.

Corresponding author: Pao-Liang Chang, larkdi@cwa.gov.tw

DOI: 10.1175/JHM-D-23-0205.1

Moreover, both Φ_{DP} and K_{DP} are immune to radar calibration, attenuation, and less sensitive to variations of DSDs (Bringi and Chandrasekar 2001; Testud et al. 2000). Consequently, many studies have shown that applying dual-polarimetric radar parameters can significantly improve the performance of radar rainfall estimation (Ryzhkov and Zrnić 2005; Chen et al. 2021; Ryzhkov et al. 2022). Ryzhkov et al. (2014) used 7-yr disdrometer data in the United States to derive relationships between rain rate R and radar variables Z, K_{DP}, and specific attenuation A. When comparing Z, K_{DP}, and A, we found that the $R(K_{\mathrm{DP}})$ relationship is less sensitive to DSD variabilities than $R(A)$ and $R(Z)$ for very high rain rates for both C and X bands, and the $R(A)$ relationship is less sensitive to DSD variabilities for the S band. The results reflect that K_{DP} and A are nearly immune to radar miscalibration, partial beam blockage, and wet radome effects. However, there are still some challenges to apply radar variables for specific relationships to estimate rainfall because of some pros and cons for each variable. For example, Z_{DR} and K_{DP} observation data were relatively noisy in light rain; the Z_{DR}-based QPE can be too sensitive to the Z_{DR} calibration and attenuation issues (Ryzhkov and Zrnić 2005; Zrnić et al. 2006; Kumjian 2013). As for $R(K_{\mathrm{DP}})$, it performs better in heavy rain QPE than $R(Z)$ but at a lower resolution due to certain filtering processes required for a robust K_{DP} estimation (Ryzhkov et al. 2014). Therefore, rainfall retrievals using a combination of relationships between R and Z, Z_{DR}, and K_{DP} according to different hydrometeor types are desired to accurately capture the DSD conditions (Cifelli et al. 2011).

Ryzhkov et al. (2014) showed that the $R(A)$ relation better captured the variability of DSDs than traditional rainfall algorithms based on Z, Z_{DR}, and K_{DP} in a wide range of rain intensity for S-band radar. However, the attenuation cannot be observed by radar directly and was computed from the ZPHI formula (Bringi et al. 1990; Testud et al. 2000). The ZPHI method had combined Z and Φ_{DP} measurement to compute attenuation. The value of attenuation is given to the optimization of the factor α used for computation of a path-integrated attenuation (PIA) from a total span of Φ_{DP} along the propagation path in rain (Wang et al. 2019). Wang et al. (2017) indicated that α in $R(A)$ algorithm plays an important role in the A field estimation for S band. The value of α was related to the normalized concentration of raindrops (Nw), temperature, and radar wavelength. The α parameter can be derived using a Z_{DR}–Z slope in real time (Wang et al. 2019; Zhang et al. 2020) and can vary with time. The usage of relative quantities (i.e., the Φ_{DP} span and Z_{DR}–Z slope) made $R(A)$-based QPE more immune to Z and Z_{DR} calibration errors. Cocks et al. (2019) indicated 26% lower errors and a 26% better bias ratio, with the QPE utilizing a real-time estimated α as opposed to using a fixed value of α as was done in previous studies. Chen at al. (2021) optimized α according to Nw and Z_{DR} slopes and conducted the regime-adapted rainfall retrievals to a C-band radar network in Europe. The rainfall retrievals significantly reduce the effects of partial beam blockage compared to all algorithms based on Z, but still some challenges result from the inhomogeneity of the precipitation regimes within the scan.

Due to the complex terrain, there are significant variations in rainfall regimes across Taiwan throughout the year (Chen and Chen 2003). The DSDs associated with various regimes are very localized and unique to Taiwan's geography and climatology (Lee et al. 2019). Chang et al. (2009) compared the DSDs from the typhoon systems in Taiwan with the DSDs from the United States in Bringi et al. (2003). It was found that, over the ocean, the typhoon rainfall DSDs were similar to the maritime convective type as defined in Bringi et al. (2003). But over the land, the Taiwan DSDs tended to be uniquely located in between the continental and maritime clusters of the U.S. DSD. Lee et al. (2019) used Joss–Waldvogel Disdrometer (JWD) observation and vertical profile of reflectivity to compare microphysical features for the different precipitation types in the summer and winter seasons of northern Taiwan. They found larger mass-weighted average diameter (Dm, Ulbrich and Atlas 1984; Testud et al. 2000) in summer but larger normalized intercept parameter (Nw, Testud et al. 2000) in winter. The climatological distribution of Dm–Nw showed that most of the rainfall types in northern Taiwan is maritime (Bringi et al. 2003; Lee et al. 2019), which was different from the Oklahoma, United States, DSD data, from which Ryzhkov et al. (2014) derived their $R(A)$ relations. The Ryzhkov et al. (2014) $R(A)$ relations are currently used in the Taiwan operational radar QPE (Chang et al. 2021).

Given the unique Taiwan DSDs found in the aforementioned studies, a study of the impact of such DSDs on the radar QPE is warranted. The current study tries to analyze the local DSDs and radar–rainfall relationships using an operational disdrometer network consisting of 27 Particle Size and Velocity (Parsivel) stations that was implemented in 2016. The network provides long-period and island-wide observations in Taiwan. With the disdrometer data, rain rates can be directly calculated and near-ground radar variables, such as Z, Z_{DR}, K_{DP}, and A, can be simulated by the T-matrix method (e.g., Waterman 1971; Barber and Hill 1990). Relationships between the simulated radar parameters and the rainfall intensity, such as $R(Z)$, $R(K_{\mathrm{DP}})$, etc., can then be derived and their performances can be compared to the previous relationships used in the Taiwan operational radar QPE products. The results will provide insights into the sensitivities of various radar–rain rate relationships to the local Taiwan DSD regimes and guidance to the improvement of the operation radar QPEs.

In the following section, the data and methodology are described. The localization of radar–rainfall relationships and a number of QPE experiments testing the impact of the local relationships using DSD data are presented in section 3. Section 4 presents additional QPE experiments using weather radar observations during mei-yu front and typhoon cases. Finally, a summary is provided in section 5.

2. Data and methodology

a. *Radar and gauge observations*

The radar data used in this study are from an S-band Weather Surveillance Radar-1988 Doppler (WSR-88D) (Miller et al. 1998) located at the Wu-Fan San site (RCWF) in northeastern Taiwan. The radar was installed in 1996 and upgraded to dual-polarization in 2014. The radar data were quality controlled with

TABLE 1. A list of cases for analyses in this study.

Periods	Events
1–4 Jun 2017	Mei-yu front
13–18 Jun 2017	Mei-yu front
22–23 Jul 2014	Typhoon Matmo
20–22 Sep 2014	Typhoon Fung-wong
7–8 Aug 2015	Typhoon Soudelor
29–30 Jul 2017	Typhoon Haitang and Nesat

a physically based scheme (Tang et al. 2014) using Z, ρ_{HV}, and temperature data to identify and remove nonprecipitation echoes. In this study, the mei-yu and typhoon cases (Table 1) are selected to evaluate several QPEs including 1) a traditional $R(Z)$, 2) a dual-pol radar synthetic QPE used in the current operational QPESUMS, and 3) the new localized QPE algorithms developed from the disdrometer observations in Taiwan.

The current study used rain gauge observations from 107 stations in northern Taiwan (Fig. 1) to verify the various radar-derived QPEs. The gauge data are quality controlled through procedures developed by Zheng et al. (2011) and Kao and Lin (2023). The procedures include temporal and spatial checks. Gauge values exceeding tipping-bucket rain gauge limits or climatological upper bounds are flagged for removal. Furthermore, radar data are used for the identification and elimination of anomalous records. To reduce the radar QPE uncertainties introduced by high radar beams, these gauges were chosen from areas where the radar beam bottom is below 2 km above the ground.

b. *Disdrometer observations*

The CWA implemented an operational disdrometer network of 27 Parsivel stations island-wide in Taiwan since 2016. The current study used 3 years (2016–18) of the data from 9 of the 27 stations in northern Taiwan (blue "O" symbols in Fig. 1) to derive localized radar–rain rate relationships. Further, a DSD dataset of Taipei station (green "O" in Fig. 1) from 2019 to 2021 was used in a number of sensitivity experiments.

The Parsivel disdrometer provides direct measurements of raindrop size and fall velocity every 1 min that can be utilized to calculate rain rate R, Dm, and Nw. The DSD data were used to simulate radar-observed variables such as Z, Z_{DR}, and K_{DP} for wavelength set 10.48 cm at 20°C. For instance, the specific attenuation A can be simulated by the T-matrix method (e.g., Waterman 1971; Barber and Hill 1990). A quality control algorithm for Parsivels based on Lu et al. (2020) is applied to remove unreasonable signals by comparing the ideal diameter–fall velocity relation (Brandes et al. 2002). This step is important since disdrometer data quality can be affected by environmental conditions, such as wind speed and wind direction (Friedrich et al. 2013a,b).

c. *R(A) algorithm*

The utilization of specific attenuation for rainfall estimation $R(A)$ can greatly benefit from the preservation of the higher spatial resolution observed in radar reflectivity data than $R(K_{DP})$, avoiding Z_{DR} noise, and reducing effects of wet radome, attenuation, and partial beam blockage. While the $R(A)$ relation is much less sensitive to DSD variations than the $R(Z)$ and $R(K_{DP})$ algorithms, errors existed and were caused by uncertainty of DSD variability when calculated A in Ryzhkov et al. (2014). Therefore, the localization for $R(A)$ formula is still important to improve the accuracy of rainfall estimation.

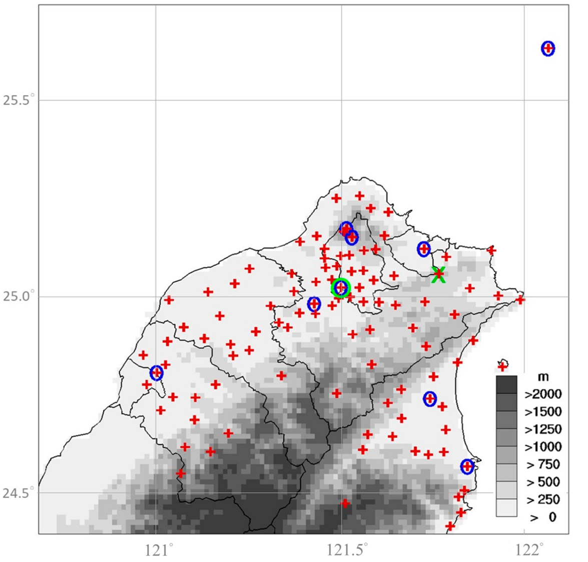

FIG. 1. The disdrometer and gauge stations in northern Taiwan are indicated in blue circles and red crosses, respectively. The Taipei station is indicated in green circle. The radar site is indicated in green "X." The shading indicates the terrain height.

The rain rate R can be estimated from A (Ryzhkov et al. 2014) as follows:

$$R(A) = \gamma A^{\Lambda}. \tag{2.1}$$

Based on disdrometer observations in Oklahoma (RAUS), the values of γ and Λ were determined as 4120 and 1.03, respectively, for S-band radar. The variable A is estimated from the radial profile of the measured Z and the total span of the differential phase using the ZPHI method (Testud et al. 2000). The value of A along radar beams can be calculated using the following formula:

$$A(r) = \frac{[Z_a(r)]^b C(b, \mathrm{PIA})}{I(r_1, r_2) + C(b, \mathrm{PIA}) I(r, r_2)}, \tag{2.2}$$

where

$$I(r_1, r_2) = 0.46b \int_{r_1}^{r_2} [Z_a(s)]^b ds, \tag{2.3}$$

$$I(r, r_2) = 0.46b \int_{r}^{r_2} [Z_a(s)]^b ds, \tag{2.4}$$

$$C(b, \mathrm{PIA}) = \exp(0.23b\mathrm{PIA}) - 1. \tag{2.5}$$

Here, $Z_a(r)$ is the reflectivity observation along the radar beam and b is 0.62. According to the definition in Bringi et al. (1990), the PIA passed through weather system can be expressed as follows:

$$\mathrm{PIA}(r_1, r_2) = \alpha[\Phi_{\mathrm{DP}}(r_2) - \Phi_{\mathrm{DP}}(r_1)] = \alpha\Delta\Phi_{\mathrm{DP}}. \quad (2.6)$$

While the $R(A)$ method is generally immune to partial beam blockage (Ryzhkov et al. 2014), there is a challenge when the beam blockage varies significantly along the integration path. The varying blockages in a radial cause uneven effects on the reflectivity Z, resulting in biases in specific A calculations [(Eq. (2.2)]. In this study, the path integration is divided into two sections for nonuniformly blocked radials and the dividing point is at the closest gate where the beam blockage reaches 30%. The two segments and 30% blockage were chosen subjectively based on a number of case analyses. While using more segments may reduce the blockage variations in each section, the smaller size of the segments can introduce more noises in the local Φ_{DP} span. The two-section approach seems to strike a balance between assuring the quality of the local Φ_{DP} span and mitigating severe biases in the $R(A)$ estimates due to the nonuniform blockages. Further refinement of the $R(A)$ QPE in areas of nonuniform beam blockages is planned for future work.

Wang et al. (2019) showed that the factor α is a function of DSD, temperature, and radar wavelength; it requires optimization for a particular rain type. For S-band radar, the value of α is directly linked to the DSD in rainfall (Wang et al. 2014, 2019; Loh et al. 2022). In contrast, Z_{DR} is a parameter that depends on the axis ratio of raindrops and infer the mean size of DSD. This sensitivity of Z_{DR} to DSD variations is useful in calculating α. By conducting long-term disdrometer analysis, it is straightforward to obtain the value of α, which provides insights into the distribution of raindrop sizes. According to Ryzhkov et al. (2014), it is recommended to use an α value of 0.015 dB per degree for S-band radar. Wang et al. (2019), through disdrometer analysis, have found that the average α value in continental rain regions is approximately 0.014 dB per degree, while in tropical rain regions, the average α value is around 0.026 dB per degree. These fixed α values represent the climatology averages for different precipitation regimes. In the operational QPESUMS (Chang et al. 2021) and the U.S. Multi-Radar Multi-Sensor (MRMS) (Zhang et al. 2020) systems, a dynamic α can be derived for each volume scan when there are enough data samples. This dynamic α is more representative of the real-time precipitation DSDs. Specifically, Wang et al. (2019) derived the following relationship (hereafter "LLUS") with the U.S. disdrometer data for α:

$$\alpha = 0.049 - 0.75K, \text{ if } K \le 0.045;$$

$$\alpha = 0.015, \text{ if } K > 0.045. \quad (2.7)$$

Here, K is the so-called "Z_{DR} slope," which is the slope of a linear line fitted to the median Z_{DR} values within each 2-dBZ reflectivity interval between 20 and 50 dBZ. Because of the derivative nature of K, α is independent of absolute biases in Z and Z_{DR} observations making it less sensitive to potential calibration biases and partial beam blockages.

In this study, the 2016–18 disdrometer data are utilized to determine the local climatological α value and to derive the coefficients of R–A and α–K relationships. The localized radar–rainfall relationships are applied to a new QPE, which are then compared with several reference radar QPEs. One of the reference QPEs is a traditional $R(Z)$ QPE (hereafter "RZOP") using the S-band $R(Z)$ relationship in the operational QPESUMS (Chang et al. 2021). The relationship is copied below for easy reference as follows:

$$R(Z) = 0.12Z^{0.61}. \quad (2.8)$$

Another reference QPE is a dual-pol radar synthetic QPE used by the RCWF radar that combines $R(A)$, $R(K_{\mathrm{DP}})$, and $R(Z)$. Ryzhkov et al. (2022) analyzed the relative advantages of the three relationships for a wide range of rain intensities. It was found that $R(A)$ typically performs better for low to moderate rain rates. In contrast, Ryzhkov et al. (2014) showed that $R(K_{\mathrm{DP}})$ was more reliable than $R(A)$ in hail cases. The synthetic QPE from RCWF takes the maximum R (rain rates) from $R(A)$ and $R(Z)$ from Eq. (2.8) for light rain (light rain is defined by $\Delta\Phi_{\mathrm{DP}} < 5°$) and uses $R(A)$ for moderate to heavy rain. When the reflectivity exceeds 50 dBZ, the following $R(K_{\mathrm{DP}})$ relationship is utilized (hereafter "RKOP," Chen et al. 2021):

$$R(K_{\mathrm{DP}}) = 47.60K_{\mathrm{DP}}^{0.76}. \quad (2.9)$$

This study aims to compare RZOP, RAOP, and RKOP with the localized radar QPEs using the metrics presented next. The description of the QPE localization efforts is provided in section 3.

d. Skill scores for performance evaluation

The QPE performances were evaluated using three scoring metrics in this study: normalized mean error (NME), relative root-mean-square error (RRMSE), and correlation coefficient (CC). These metrics provide a quantitative assessment of how well the curve fitting algorithms perform in terms of accuracy, precision, and the relationship between predicted and observed values

$$\mathrm{NME} = \frac{\sum_{i=1}^{N}(Q_i - G_i)}{\sum_{i=1}^{N} G_i}, \quad (2.10)$$

$$\mathrm{RRMSE} = \frac{\sqrt{\dfrac{\sum_{i=1}^{N}(Q_i - G_i)^2}{N}}}{\sqrt{\dfrac{\sum_{i=1}^{N} G_i^2}{N}}}, \quad (2.11)$$

$$\mathrm{CC} = \frac{\sum_{i=1}^{n}(Q_i - \underline{Q_i})(G_i - \underline{G_i})}{\sqrt{\sum_{i=1}^{n}(Q_i - \underline{Q_i})^2 \sum_{i=1}^{n}(G_i - \underline{G_i})^2}}, \quad (2.12)$$

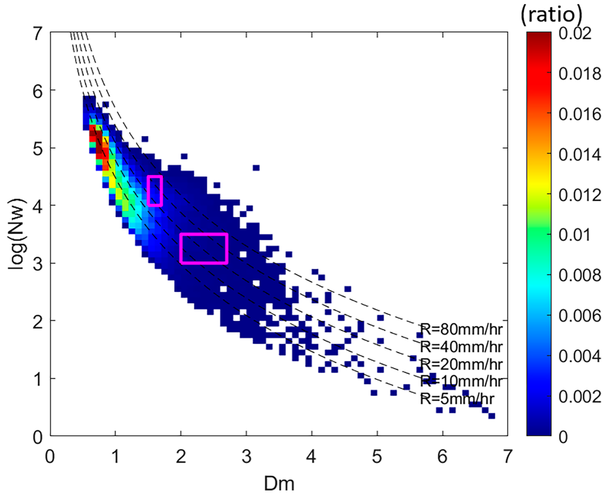

FIG. 2. Frequency distribution of Dm and log(Nw) in northern Taiwan. The pink boxes represent the marine (left box) and continental (right box) regimes based on Bringi et al. (2003). The dashed line denotes the rain rate.

where Q, G, and N are the values of the QPE estimation, rain gauge observation, and sample number, respectively. The positive value of NME indicates the radar QPE overestimation and vice versa. The larger absolute values of NME indicate worse performance for the estimation. On the other hand, a smaller RRMSE value indicates better performance. If the CC value is close to 1, it indicates a high level of agreement or similarity between the observation and estimation.

3. Localization of QPE relationships

a. *Characteristic of DSD in Taiwan*

The characteristics of the 2016–18 Parsivel DSD data from the nine stations in northern Taiwan were analyzed following several previous studies (Chang et al. 2009; Lee et al. 2019; Chen et al. 2021) of similar efforts. Figure 2 shows the frequency distribution of the Dm and the logarithm of Nw in northern Taiwan, in which the two pink boxes represent the marine and continental rainfall types as defined in Bringi et al. (2003). For the continental (marine) type, Dm values are typically between 2 and 2.75 (1.5 and 1.75) and log(Nw) ranges from 3 to 3.5 (4 and 4.5). In the Taiwan DSD dataset, a majority population (frequency > 0.01 in Fig. 2) is centered at Dm below 1.5 mm and log(Nw) between 4 and 4.5, indicating a lot of smaller raindrops in Taiwan than in the two regimes defined in Bringi et al. (2003). And the majority of the rain rates were mostly below 10 mm h^{-1}. The DSD data were also segregated for two specific rainfall regimes of mei-yu and typhoons, which are two major contributors of the heavy rainfalls in Taiwan (Lee et al. 2019). Mei-yu is a distinctive phenomenon of East Asia and ranks among the most impactful weather systems in China and its surrounding regions (Chen 2004). These quasi-stationary fronts typically precede the seasonal transition in mid-June and are frequently associated with the onset and progression of mesoscale convective systems (Chen 1992; Chen 1993; Zhang et al. 2019). The intense convective storms often result in heavy rainfall, lightning, and hail, leading to frequent and significant flood disasters in Taiwan. The typhoon dataset corresponds to the period when the CWA issued typhoon warnings from 2016 to 2018 and the mei-yu dataset was extracted from the months of May and June. While the mei-yu DSD (Fig. 3a) had many small raindrops below 1 mm that was similar to the overall northern Taiwan DSD (Fig. 2), there is another high-concentration cluster of Dm between 1 and 1.5 mm and log(Nw) between 3.5 and 4.5 (white "X," Fig. 3a). The typhoon season DSD (Fig. 3b) had much fewer samples than those in the mei-yu season and a high-concentration cluster with smaller drops of Dm between 1 and 1.2 mm and log(Nw) between 3.8 and 4.3 (white "X," Fig. 3b). Both the mei-yu and typhoon DSDs are distinctly different from the two clusters in Bringi et al. (2003), with higher concentrations of smaller drops than the latter.

b. *Localization of α(K)*

As mentioned above, the $R(A)$ QPE in the current QPESUMS (Taiwan) and MRMS (United States) system

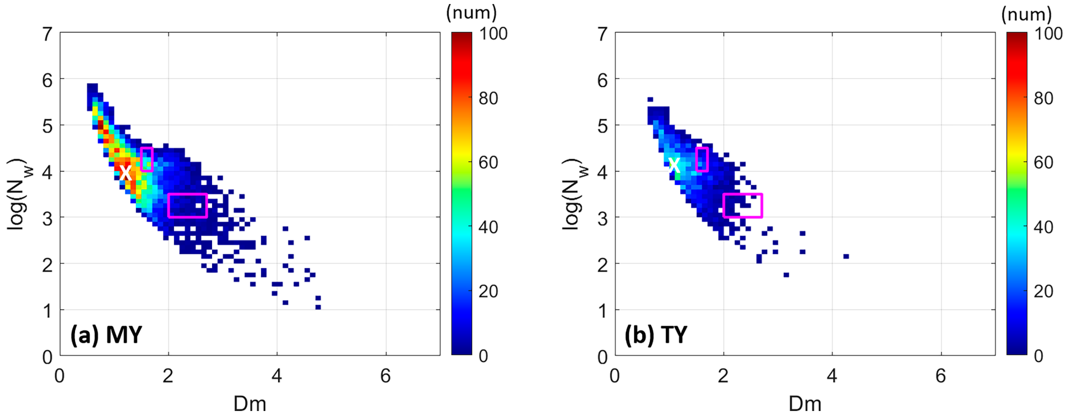

FIG. 3. The number distributions between Dm (mm) and log(Nw) ($\mathrm{mm}^{-3}\ \mathrm{m}^{-1}$), the dataset from (a) mei-yu and (b) typhoon events. The white "x" symbols indicate the maximum number concentrations.

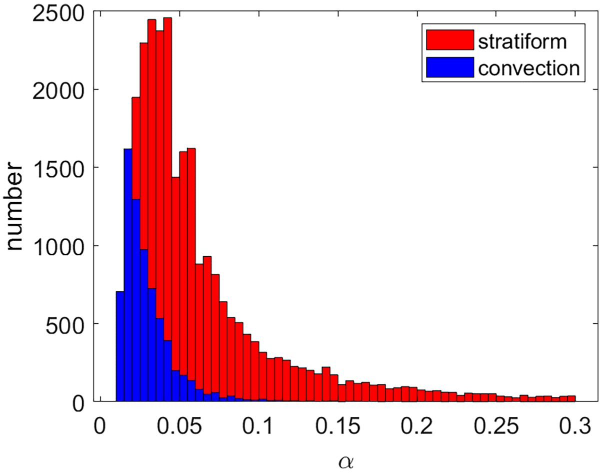

FIG. 4. Histograms of α values derived from 3-yr (2016–18) DSD data in northern Taiwan. The locations of the disdrometers are shown in Fig. 1. Blue bars represent convective events and red bars are stratiform.

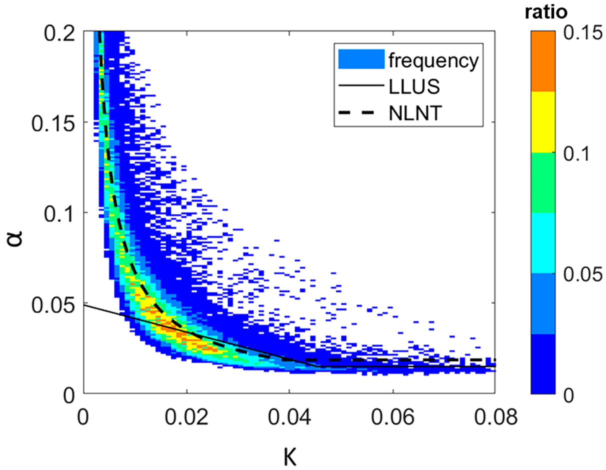

FIG. 5. Scatterplot between α and K derived from 3-yr (2016–18) DSD dataset in northern Taiwan (see locations of the disdrometers in Fig. 1). The shading represents the number ratio between the data in a given α–K bin and the total data. The dashed line represents the relationship derived from the DSD data in northern Taiwan, and the solid line indicates the relationship between α and K derived from Wang et al. (2019).

derives the α parameter dynamically from a linear function of the Z_{DR} slope K in real time. To assure a robust and representative Z_{DR} slope, a large number of Z and Z_{DR} data samples are required in the radar observation areas below the melting layer. The data samples from areas where the radar beam is within or above the melting layer are not used because the $R(A)$ relation is only valid in a pure liquid environment. When there are not enough radar data samples below the melting layer, such as in small isolated thunderstorms or when the precipitation echoes are far away from the radar, a predefined α value is needed for $R(A)$ calculations. Zhang et al. (2020) used a default convective (0.015) or stratiform (0.035) α values for the $R(A)$ QPE in the MRMS system depending on the reflectivity intensities and areal coverage.

In the current study, α values were derived from the 3-yr Parsivel data of nine stations in northern Taiwan. The DSD data were used to simulate the radar variables of A and K_{DP} by the T-matrix method. The value of α was calculated by the ratio of A and K_{DP} and was segregated for convective and stratiform precipitation. The precipitation segregation was based on three-dimensional mosaic reflectivity data from the QPESUMS using the method by Steiner et al. (1995). Figure 4 presents the histogram of the disdrometer-derived α values for convective and stratiform precipitation types, indicating the median values of α to be 0.024 for convective and 0.048 for stratiform. These are clearly higher than the default values from the U.S. precipitation systems and should be considered for the $R(A)$ QPE in Taiwan.

Figure 5 shows the scatterplot between α and K derived from 3-yr northern Taiwan disdrometer observations. Similar to α, K was calculated from the Z and Z_{DR} values simulated from the DSD data via the T-matrix method. The distribution of the dataset numbers reveals that the majority of the data is concentrated within the range of K values between 0.01 and 0.03, indicating that there were larger quantities of small rain droplets within the precipitation system in northern Taiwan. Subsequently, the following nonlinear northern Taiwan (NLNT) $\alpha(K)$ relation is proposed to better represent the characteristic of local DSD:

$$\alpha = 0.0009K^{-0.9361}, \text{ if } K \le 0.0387;$$

$$\alpha = 0.0187, \text{ if } K > 0.0387. \tag{2.13}$$

It is noted that the α value from LLUS [Eq. (2.7)] was limited within the range of 0.049 and 0.015. This is a very narrow distribution compared to the α values derived from the Taiwan local disdrometer data (Fig. 5). The LLUS $\alpha(K)$ relation (solid line in Fig. 5) appears to be lower than the disdrometer-simulated α values when K is less than 0.018 but higher for $K = 0.02$–0.04. This difference implies that the $R(A)$ scheme based on LLUS $\alpha(K)$ relation will likely have a dry bias for very small K values (i.e., rainfall consists of mostly small drops) and a wet bias for medium K values (i.e., rainfall with mixed small and medium drops). On the other hand, the NLNT relationship (dashed line, Fig. 5) captures the α distribution much better than the LLUS. Figure 6 shows the distribution of K in mei-yu fronts and typhoon systems, which are two major contributors to heavy rain in Taiwan, and associated QPE experiments with the LLUS and NLNT will be presented next.

c. *Localization of radar variable–rain rate relationships*

The 2016–18 disdrometer dataset from the nine stations in northern Taiwan was used to fit the local $R(Z)$, $R(K_{\mathrm{DP}})$, and $R(A)$ relationships as follows:

$$\mathrm{RZNT}: R(Z) = 0.076Z^{0.57}, \tag{2.14}$$

$$\mathrm{RKNT}: R(K_{\mathrm{DP}}) = 48.44K_{\mathrm{DP}}^{0.71}, \tag{2.15}$$

$$\mathrm{RANT}: R(A) = 3390A^{1.02}. \tag{2.16}$$

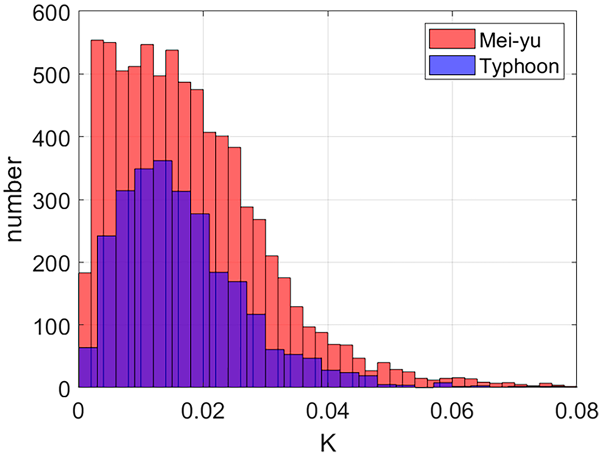

FIG. 6. Histogram of Z_{DR} slope K simulated from the 3-yr (2016–18) DSD dataset in northern Taiwan (see locations of the disdrometers in Fig. 1). Red bars represent mei-yu front, and blue bars represent typhoon events.

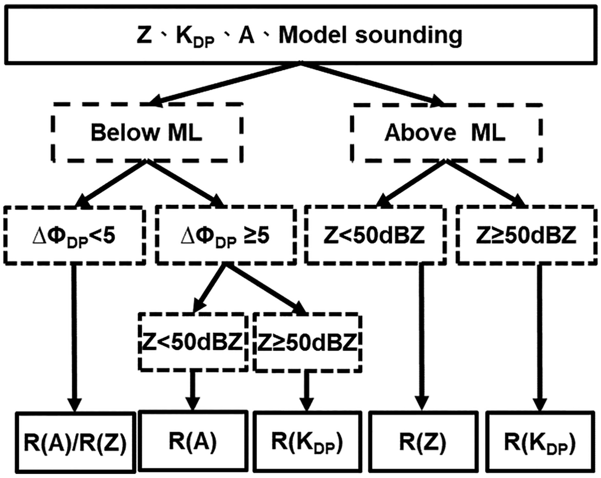

FIG. 7. The flowchart of the dual-pol radar synthetic QPE. Detailed descriptions can be found in the text.

Comparing Eqs. (2.14)–(2.16) with Eqs. (2.8), (2.9), and (2.1), respectively, the $R(A)$ relationships stayed very close to linear for both United States [exponent = 1.03, Eq. (2.1)] and Taiwan [exponent = 1.02, Eq. (2.16)]. The difference in the multipliers [4120 in Eq. (2.1) versus 3390 in Eq. (2.16)] was largely due to the difference in the wavelengths [11.0 cm for Eq. (2.1) and 10.48 cm for Eq. (2.16)].

d. *Synthetic QPE*

For rainfall estimation, different radar variables have their strengths and weaknesses. For example, deriving accurate K_{DP} and A can be challenging in light rain conditions due to the low attenuation signals. On the other hand, Z is generally more stable and reliable. To account for these strengths and weaknesses, the operational QPESUMS system in Taiwan used a synthetic rainfall estimation that combines $R(A)$, $R(K_{\mathrm{DP}})$, and $R(Z)$ (hereafter "SYNOP"). This approach, initially proposed by Zhang et al. (2020) and further refined by Chang et al. (2021), improves the rainfall estimation across various weather conditions over its predecessor that is based on $R(Z)$ only. Figure 7 shows a flowchart of the synthetic QPE scheme. Due to the applicability of $R(A)$ exclusively in the liquid precipitation region, a melting layer delineation is necessary to segregate the radar observation into sections of pure liquid and otherwise. The determination of the melting layer height in QPESUMS was based on the 3D temperature field from Space and Time Multiscale Analysis System (STMAS) (Xie et al. 2005, 2011). And $R(A)$ is only applied in the radar observation areas below the melting layer. Further, $R(A)$ application is constrained to areas of $\Delta\Phi_{\mathrm{DP}} \geq 5°$ and $Z < 50$ dBZ to avoid hail contamination and the potential $R(A)$ errors associated with very low attenuation signals. Within and above the melting layer, $R(Z)$ is utilized for the rainfall estimation. For reflectivity values exceeding 50 dBZ, which often suggest the existence of ice-phase particles like hail, $R(K_{\mathrm{DP}})$ is applied. When the precipitation intensity is weak and there are minimal changes in the phase difference ($\Delta\Phi_{\mathrm{DP}} < 5°$), it becomes challenging to obtain accurate A and K_{DP} data. In such cases, the maximum value from $R(Z)$ and $R(A)$ is selected for analysis. Table 2 lists two sets of radar–rainfall relationships that are used in the synthetic QPE scheme. The SYNOP set is the current operational QPESUMS relationship, and SYNNT represents the synthetic QPE based on localized relationships derived from disdrometer data in northern Taiwan. The two sets of relationships are applied in a series of QPE experiments, and the results are discussed in the following sections.

e. *QPE experiments*

1) INDIVIDUAL RADAR VARIABLE–RAIN RATE RELATIONSHIPS

A set of QPE experiments were carried out using the local $R(Z)$, $R(A)$, and $R(K_{\mathrm{DP}})$ relationships versus their counterparts in the QPESUMS. The experiments derived rain rates R using the A, Z, and K_{DP} data simulated from 3 years (2019–21) of disdrometer data from the Taipei station using the given relationships. These rain rates R are compared with the rain rates directly calculated from the disdrometer observations. The localized relationships provided better performance than the operational ones with smaller RRMSE and higher CC (Table 3). Among the three localized relationships, $R(A)$ is superior to both $R(K_{\mathrm{DP}})$ and $R(Z)$ based on CC (0.9899 vs 0.9673 and 0.9277). This is consistent with the findings in Ryzhkov et al. (2014), where $R(A)$ estimates have the least uncertainty. The term $R(K_{\mathrm{DP}})$ provided ~13% improvement over $R(Z)$ in RRMSE (0.2214 vs 0.3551), and $R(A)$ provided an additional 9.7% improvement (0.1241 vs 0.2214).

Figure 8 shows the RRMSE values from various QPE experiments as a function of the DSD precipitation intensities every 5 mm h^{-1}. RZOP consistently produced the highest RRMSEs and largest overestimations across all rainfall intensities, while the localized $R(Z)$ relation (RZNT) performed significantly better. The huge difference between the two $R(Z)$ QPEs may be largely related to the vertical variations of

TABLE 2. Radar–rain rate relations and default α values in the operational (SYNOP) and new localized (SYNNT) synthetic QPEs. The default α values were for three different weather regimes, i.e., convection, stratiform and mixed rain.

	SYNOP	SYNNT
$R(K_{\mathrm{DP}})$	$R(K_{\mathrm{DP}}) = 47.60K_{\mathrm{DP}}^{0.76}$	$R(K_{\mathrm{DP}}) = 48.44K_{\mathrm{DP}}^{0.71}$
$R(A)$	$R(A) = 4120A^{1.03}$	$R(A) = 3390A^{1.02}$
$R(Z)$	$R(Z) = 0.12Z^{0.61}$	$R(Z) = 0.076Z^{0.57}$
$\alpha(K)$	$\alpha = 0.049–0.75K$, if $K \le 0.045$	$\alpha = 0.0009K^{-0.9361}$, if $K \le 0.0387$
	$\alpha = 0.015$, if $K > 0.045$	$\alpha = 0.0187$, if $K > 0.0387$
Default α	$\alpha_{\mathrm{con}} = 0.015$, $\alpha_{\mathrm{mix}} = 0.025$, $\alpha_{\mathrm{str}} = 0.035$	$\alpha_{\mathrm{con}} = 0.024$, $\alpha_{\mathrm{mix}} = 0.036$, $\alpha_{\mathrm{str}} = 0.048$

reflectivities in orographically forced precipitation. RZOP was derived from weather radar observations and gauge data (Chang et al. 2021) and somewhat implicitly accounted for the vertical variations of reflectivity. On the other hand, RZNT was fit to the Z and R from the same DSD dataset at the ground and vertical variation of reflectivity was not a factor, thus the large differences between the RZNT and RZOP. The effect of vertical variations of reflectivity is more pronounced in the cold season because rain intensities in the winter precipitation systems of Taiwan tend to be lighter than in the warm season and $R(Z)$ is used more often in the synthetic QPE. The term $R(Z)$ is more sensitive to DSD variabilities in the vertical, and its performance degrades when the terrain blockage forces the usage of Z data from higher altitudes.

In terms of RRMSE (Fig. 8a), all polarimetric relations outperformed the $R(Z)$. The localized RANT relation performed significantly better than the RAUS relation, while the two $R(K_{\mathrm{DP}})$ relationships, RKOP and RKNT, performed very similarly (Fig. 8a). In terms of NME, both RZOP and RAUS showed overestimation (Fig. 8b) across all rain rates, with RZOP much worse. Among the localized relations, RZNT had the largest biases and RANT had the smallest (below 7% for all intensities). For the $R(K_{\mathrm{DP}})$ experiments, RKOP and RKNT performed similarly in RRMSE (pink lines, Fig. 8a), but the localized RKNT had less biases for rainfall below 50 mm (Fig. 8b). Above 50 mm, both $R(K_{\mathrm{DP}})$ relationships performed similarly and had underestimation (Fig. 8b).

2) $\alpha(K)$

A special experiment was designed to compare the United States and the local $\alpha(K)$ relationships using the disdrometer data from Taipei station. Time series of rain rate R and specific attenuation A were derived from Z, Z_{DR}, and K_{DP} simulated from the 3-yr disdrometer data using the T-matrix method. The Z and Z_{DR} values from every 10 min of DSD data were treated as a single gate, and every 144 gates were combined into a single "radial." Therefore, a total of 1096 simulated radar radials were composed from the 2019–21 disdrometer data. Figure 9 shows the experimental design for the $\alpha(K)$ evaluations. First, the Z_{DR}-slope K was calculated from the disdrometer retrieved Z and Z_{DR}, and then, the parameter α is calculated from K using LLUS and NLNT, respectively. The α was then used to calculate A at each "gate" within the simulated radials. Finally, rain rates were calculated using the RAUS and RANT with different $\alpha(K)$ relationships and were compared to the rate derived from the DSD data directly.

TABLE 3. The verification scores are based on different radar–rain rate relationships.

	RRMSE	CC	NME
RANT	0.1241	0.9899	−0.0064
RAUS	0.2152	0.9894	0.1407
RKNT	0.2214	0.9673	0.0274
RKOP	0.2163	0.9702	−0.0873
RZNT	0.3551	0.9277	−0.0334
RZOP	1.2435	0.9307	1.0799

Table 4 shows the overall verification scores of rain rates calculated by the operational and localized $\alpha(K)$ and $R(A)$ relationships with respect to the DSD-observed rain rates. The localized $\alpha(K)$ function significantly improves the rainfall estimation, with a 13% reduction in the NME. In contrast, the difference between RAUS and RANT is less pronounced, with a variation of less than 1% in NME.

Figure 10 shows the performance of the different combinations of $R(A)$ and $\alpha(K)$ relationships versus the DSD-observed rain rate for categorized rain rate intensities. Both the RANT (dark blue bars, Fig. 10) and RAUS (aqua blue bars, Fig. 10) with the NLNT $\alpha(K)$ relationship yielded lower RRMSE and NME than their counterparts with the LLUS $\alpha(K)$ (green and yellow bars, respectively, Fig. 10) for all intensities, except for a slightly lower RRMSE in RANT_LLUS for the lightest rain rate category. These results are consistent with the scores in Table 1 and indicate the critical role of α in the $R(A)$ QPE. In contrast, RAUS and RANT with the same $\alpha(K)$ relations performed more similarly for most of the intensity categories, with the localized RANT performing moderately better in the 15 and 40+ mm h^{-1} categories and RAUS slightly better in the 20 mm h^{-1} categories. Overall, the localized RANT_NLNT QPE scheme showed the most robust performance and the best scores among all experiments based on the DSD data.

4. Case studies and discussion

In addition to the QPE experiments with the DSD data, the operational and localized radar–rainfall relationships were applied to the RCWF radar observations of mei-yu and typhoon cases. A total of six events (Table 1) were selected to compare three different rainfall estimation algorithms: $R(Z)$, $R(A)$, and synthetic QPE.

Figure 11 shows scatterplots of hourly rainfalls from six different QPE schemes versus gauge observations for mei-yu

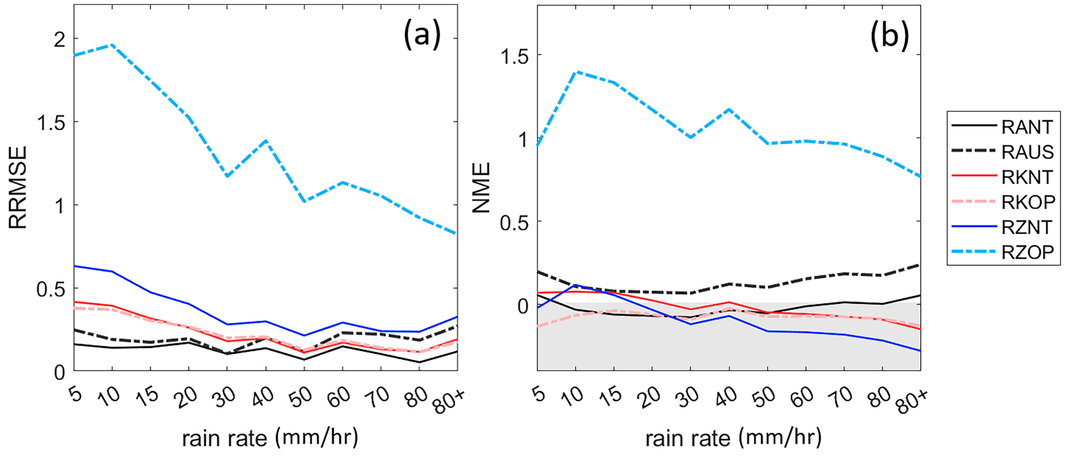

FIG. 8. (a) RRMSE and (b) NME scores of QPE experiments based on individual radar–rain rate relationships from the operational system (RZOP, RKOP, and RAOP) and from the 3-yr (2019–21) DSD data from the Taipei station (RZNT, RKNT, and RANT).

cases. The synthetic QPEs (SYNNT and SYNOP, Figs. 11a,d) outperformed individual radar–rainfall relationships and the localized scheme (SYNNT) improved upon the SYNOP by reducing the overestimation at moderate amounts (20–50 mm). Both $R(A)$ schemes (Figs. 11b,e) showed relatively larger scatters but lower biases than $R(Z)$-based schemes (Figs. 11c,f). The lower biases are likely an indicator of the more linear correlation between the specific attenuation and the total liquid water content than other radar variables. The larger scatter may be related to the uncertainties in the specific attenuation estimates, especially in relatively light rain. The performances of the two $R(Z)$ schemes (Figs. 11c,f) were somewhat counterintuitive at first, with the localized $R(Z)$ significantly underestimating the rainfall for nearly all intensities. The poor performance of RZNT with RCWF radar data was most likely a vertical profile of reflectivity (VPR) issue as discussed earlier in section 3d and in Chang et al. (2021). Since RZNT was derived from Z and R of the same DSD dataset, it does not account for height differences between the reflectivity (i.e., RCWF observations aloft) and the gauge (at the ground). RZOP, on the other hand, was chosen for the operational QPE to account for this vertical variation of reflectivity. In mei-yu events, such vertical variations can be significant with the coalescence growth of rainfall near the ground that are undetected by the radar observations aloft.

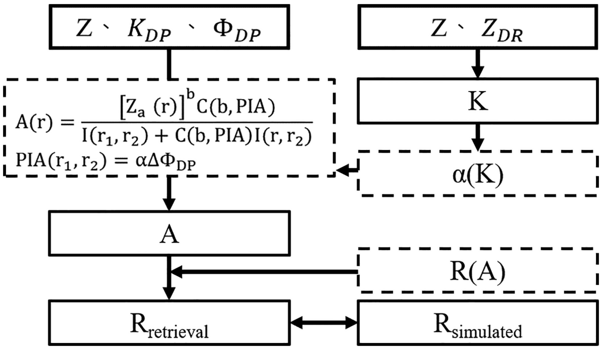

FIG. 9. Flowchart of the $\alpha(K)$ experiments. The dashed line boxes indicate formula and functions, and solid line boxes represent the variables derived from disdrometer data.

Figure 12 shows the performance of the six QPE schemes segregated for different rainfall amount categories. The two synthetic QPEs performed better than the other four individual radar–rain rate relationships (Figs. 12a,b). However, the SYNOP had an apparent wet bias for light rain below 10 mm (Fig. 12b) and a relatively high RRMSE (Fig. 12a), which was mitigated by the localized synthetic QPE (SYNNT, Figs. 12a,b). The two $R(A)$ schemes performed similarly for the light (<20 mm) and heavy (>60 mm) rainfalls, but in the middle range (20–60 mm), RAUS had a wet bias (Fig. 12b) and larger RRMSE (Fig. 12a). These midrange hourly rainfalls may be dominated by DSDs that are specific to the Taiwan areas and are not well represented by the $R(A)$ relationship derived from the United States, thus demonstrating the need to use localized radar–rainfall relationships for a higher QPE accuracy. However, the localized $R(Z)$ QPE (RZNT) had the worst dry biases across all rainfall amounts and the largest RRMSEs for rainfall amounts greater than 15 mm. As discussed earlier, this poor performance of RZNT was likely due to the vertical variations of reflectivity.

Figure 13 shows scatterplots of hourly rainfalls from six different QPE schemes versus gauge observations for the typhoon cases. All QPEs showed greater variability compared to the mei-yu cases with larger RRMSE values (Fig. 13. vs Fig. 11). Similar to the mei-yu cases, the synthetic QPEs outperformed individual relationships with the lowest RRMSE

TABLE 4. The verification scores for a 10-min averaged rain rate (mm h^{-1}).

RRMSE/NME	RAUS	RANT
LLUS	0.4646/−0.4299	0.4609/−0.4234
NLNT	0.3594/−0.2947	0.3567/−0.2893

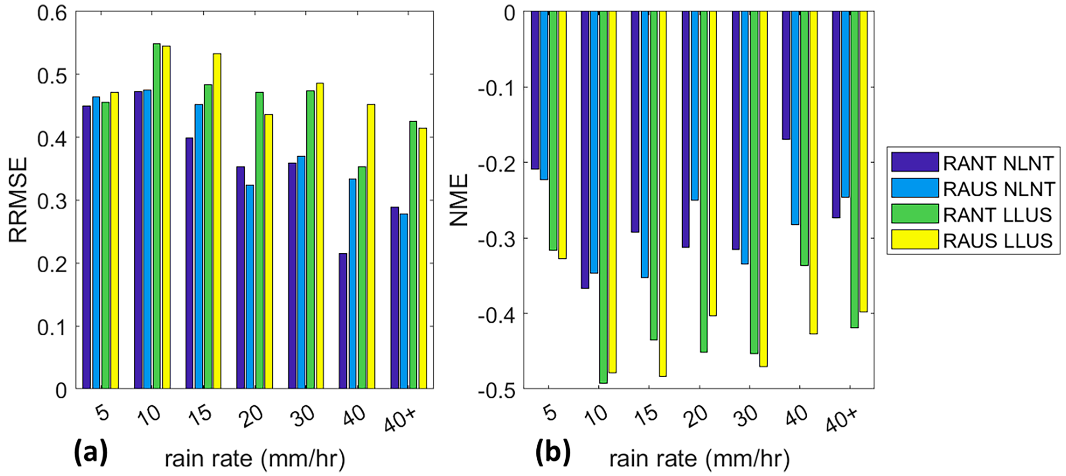

FIG. 10. (a) RRMSE and (b) NME scores of QPE experiments with different $R(A)$ and α–K relationship combinations. RANT (RAUS) represents the $R(A)$ relationship derived from the Taiwan (central United States) disdrometer data. And NLNT (LLUS) represents the nonlinear (linear) α–K relationship from the Taiwan (United States) disdrometer data. Further details can be found in the text.

and highest CC (Figs. 13a,d), and the localized $R(A)$ (RANT) with the localized $\alpha(K)$ (NLNT) relationship outperformed the operational $R(A)$ (RAUS) and $\alpha(K)$ (LLUS) (Figs. 13b,e). The relative $R(Z)$ performances, however, are different from those in the mei-yu cases. Both the operational (RZOP) and local (RZNT) relationships had significant biases, with the former an overestimation (NME = 0.3222, Fig. 13f) and the latter an underestimation (NME = −0.3713, Fig. 13c). And the two $R(Z)$ schemes yielded mixed but similar performances in terms of RRMSE (RZOP = 0.6100 vs RZNT = 0.6051) and CC scores (RZOP = 0.7277 vs RZNT = 0.7075).

When segregated for different rainfall intensities (Fig. 14), RZNT has the smallest RRMSE values for hourly rainfalls below 15 mm where RZOP has the largest (Fig. 14a). As the hourly rainfall increases, the RRMSE of RZNT increases, while the RZOP decreases, resulting in a significant difference

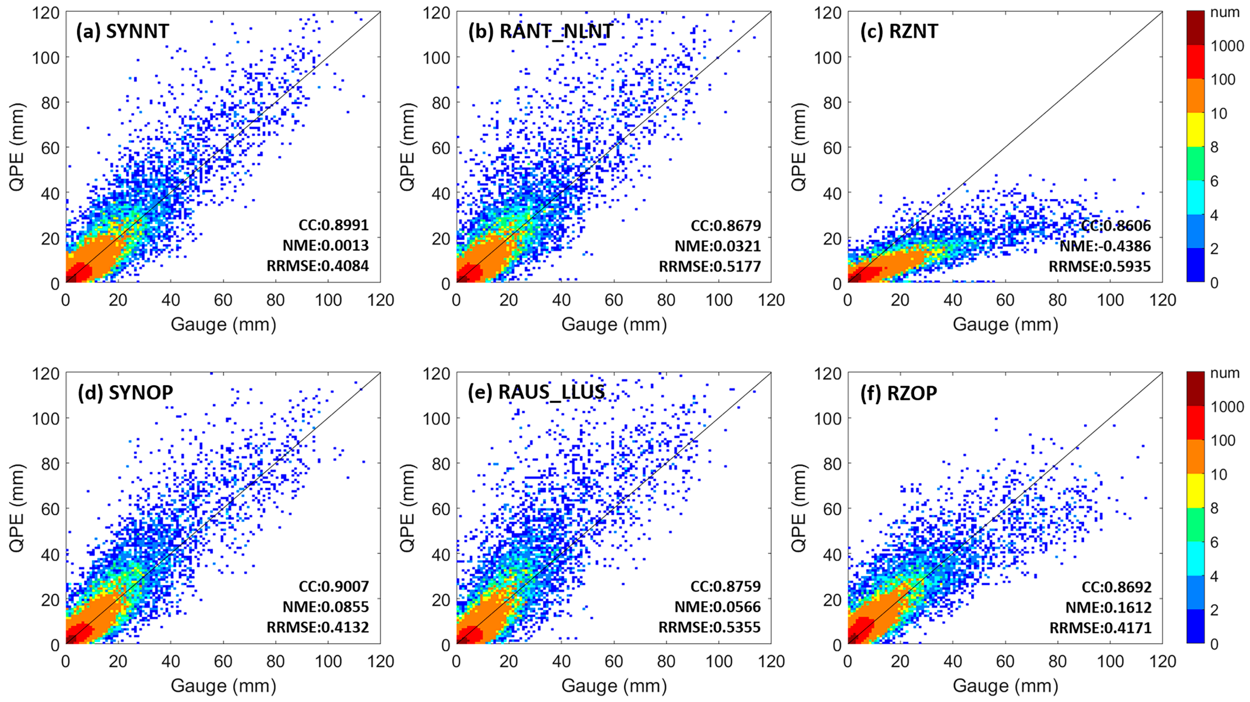

FIG. 11. Scatterplots of the hourly accumulated rainfall between gauge observations and radar estimation for mei-yu events from (a) SYNNT, (b) RANT_NLNT, (c) RZNT, (d) SYNOP, (e) RAUS_LLUS, and (f) RZOP.

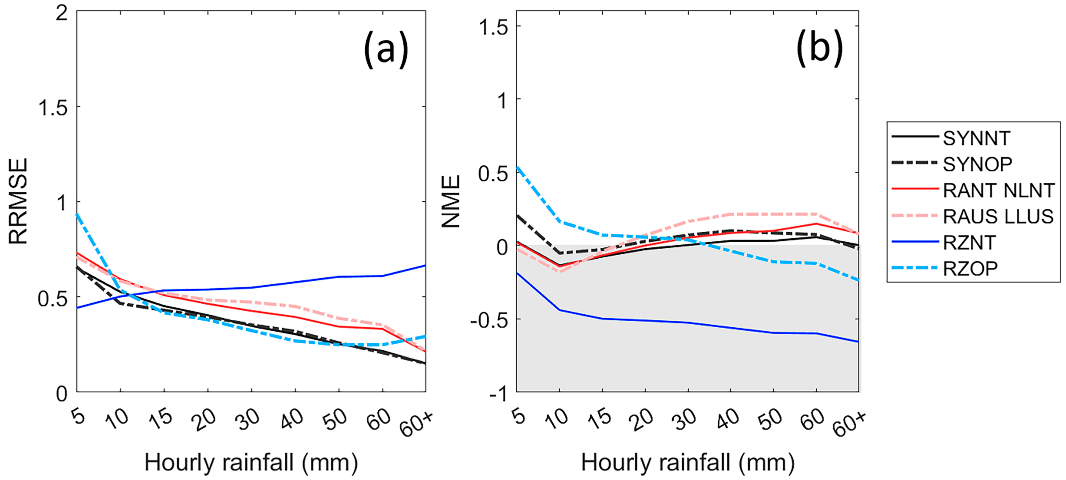

FIG. 12. Performance scores of six QPE schemes during mei-yu events for different rainfall intensities: (a) RRMSE and (b) NME.

between the two for heavy rain (solid blue vs dashed cyan lines, Fig. 14a). This is a result of the operational $R(Z)$ being chosen to better represent heavy typhoon rainfalls including the vertical variations of reflectivity before the S-band radars were upgraded to polarimetric. Further, both $R(Z)$ relationships showed an intensity-dependent bias trend (solid blue and dashed cyan lines, Fig. 14b), especially the operational $R(Z)$ with large overestimation for light rain and underestimation for heavy rain (dashed cyan line, Fig. 14b). With the polarimetric capabilities, both $R(A)$ relationships showed little such dependency (solid and dashed red lines, Fig. 14b). While the localized $R(Z)$ shows better performance for light rain with smaller RRMSE and NME (solid blue lines, Figs. 14a,b), the localized $R(A)$ shows a clear advantage for heavy rain, reducing the RRMSE for rainfall over 30 mm (solid red versus solid blue lines, Fig. 14a) and nearly eliminated all the dry biases except for the category of 60+ mm (Fig. 14b). These intensity-dependent performances of various radar–rain rate relationships demonstrate the need for a synthetic QPE. When $R(Z)$, $R(K_{DP})$, and $R(A)$ merged, the localized synthetic QPE (SYNNT) reduced the RRMSE for all ranges (solid vs dashed black lines, Fig. 14a) but introduced

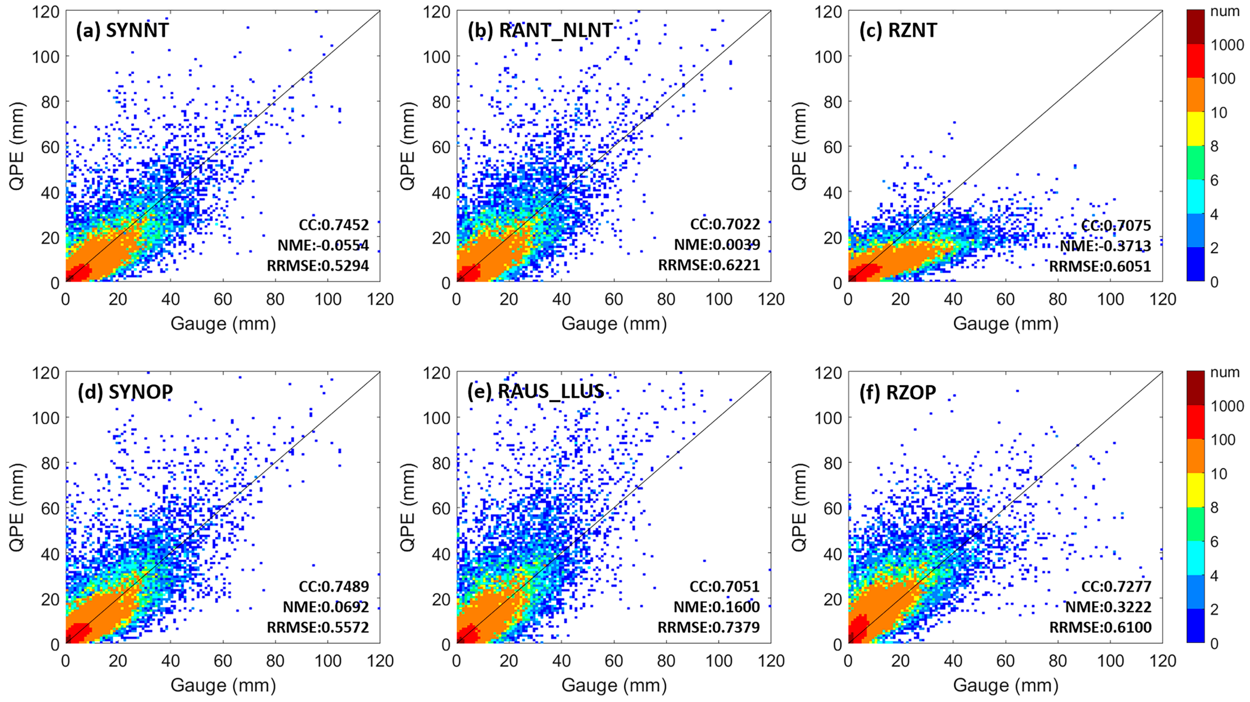

FIG. 13. As in Fig. 11, but for typhoon cases.

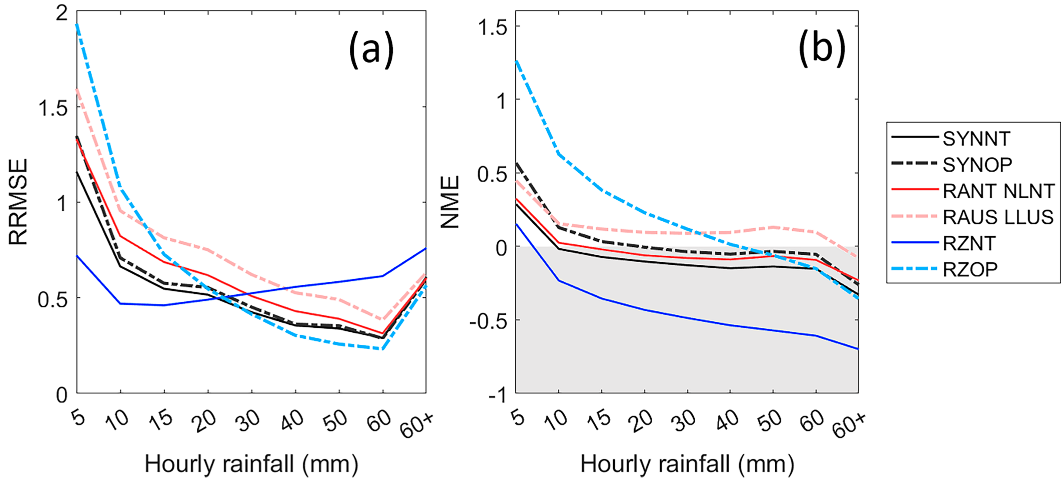

FIG. 14. As in Fig. 12, but for typhoon cases.

an underestimation bias for hourly rainfalls above 10 mm (Fig. 14b). This bias difference was not seen in the mei-yu events (Fig. 12b) and was potentially due to the local $R(A)$ relationship being dominated by the large mei-yu data samples in the DSD data (Fig. 3) from which the local relationships were derived. Further studies may be needed to refine these relationships.

It was speculated that the underestimation for 60+ mm (Fig. 14b) might be related to very heavy rain and the current $R(K_{DP})$ relationship, derived from large DSD data encompassing moderate and light rain, did not represent the very heavy regime well. Smith et al. (2023) reported a 40% negative bias in the estimate of extreme rainfall if the multiplier 44 is used in $R(K_{DP})$. Li et al. (2023) also found a strong underestimation of extreme rainfall in China and found that the multiplier in the $R(K_{DP})$ relation should be at least 70. To examine such an impact, two additional synthetic QPEs with the following high-multiplier $R(K_{DP})$ relationships from You et al. (2014) and Li et al. (2023) were applied:

$$R(K_{DP}) = 54K_{DP}^{0.867}, \tag{4.1}$$

$$R(K_{DP}) = 70K_{DP}^{0.86}. \tag{4.2}$$

However, little difference (<1%) was found in the resultant NME scores (not shown). This insensitivity to $R(K_{DP})$ may be due to the limited areas of reflectivities above 50 dBZ in the typhoon events used in the current study. Further, the severe blockages in the study region may have reduced the reflectivity intensities, resulting in the limited usage of $R(K_{DP})$. Therefore, the underestimation in Fig. 14b is mostly due to inaccuracies in $R(A)$ estimates and warrants further investigations. To examine the full impact of high-multiplier $R(K_{DP})$ relationships, it may require lowering the reflectivity threshold (50 dBZ) for $R(K_{DP})$ applications.

The larger variabilities in the typhoon QPEs were likely due to strong winds in the corresponding atmospheric environment. Due to the height differences between the RCWF radar observations and the gauge sites, the strong winds can cause significant drifts of raindrops while they fall from the radar observational height to the ground, causing discrepancies between the single-pixel radar QPE and the gauge right underneath. These discrepancies can result in unrepresentative verification results if a single radar pixel to gauge comparison is applied. To mitigate the impact of such uncertainties, a spatial relaxation technique is developed in the verification where each gauge observation is compared to an averaged radar QPE over the gauge's neighborhood area instead of a single radar QPE pixel right over the gauge.

Figure 15 illustrates the verification results of SYNNT after applying a roughly 3 km × 3 km ("3 × 3") and 5 km × 5 km ("5 × 5") neighborhood spatial relaxation. During mei-yu events, the 3 × 3 (Fig. 15a) and 5 × 5 (Fig. 15b) averaged radar QPE showed better agreement with the gauges than the pixel-to-pixel comparison (Fig. 11a), especially for heavy rainfalls. The spatial relaxation also reduced the scatter between the radar QPEs and gauge observations for typhoon events (Figs. 15c,d vs Fig. 13a). However, significantly larger errors still remain in the radar QPEs in typhoons than in mei-yu events (Fig. 15d vs Fig. 15b) even with the spatial average. To better understand these errors, the gauge locations with high frequencies of large hourly QPE–gauge differences (i.e., >30 mm) are plotted in Fig. 16. The red "O" symbols indicate locations with significant radar QPE overestimation, and the blue "X" symbols underestimate. Most of these QPE–gauge data pairs were from the heavy rain of Typhoon Soudelor (7–8 August 2015) and they are mostly in the complex terrain. The errors were most likely due to an estimation error of A in areas of highly nonuniform beam blockages. The uniformity of blockages in a given radial is crucial, as the A estimation at a given gate depends on the ratio of the reflectivity at the gate to the integration of reflectivities over the path [Eqs. (2.2)–(2.6)]. Regions with fewer blockages tend to yield higher A estimation than heavily obstructed sections along the integration path [Eqs. (2.6)]. This result indicated that the radial segmentation scheme in the current $R(A)$ scheme requires further refinement and will be a focus of our future work.

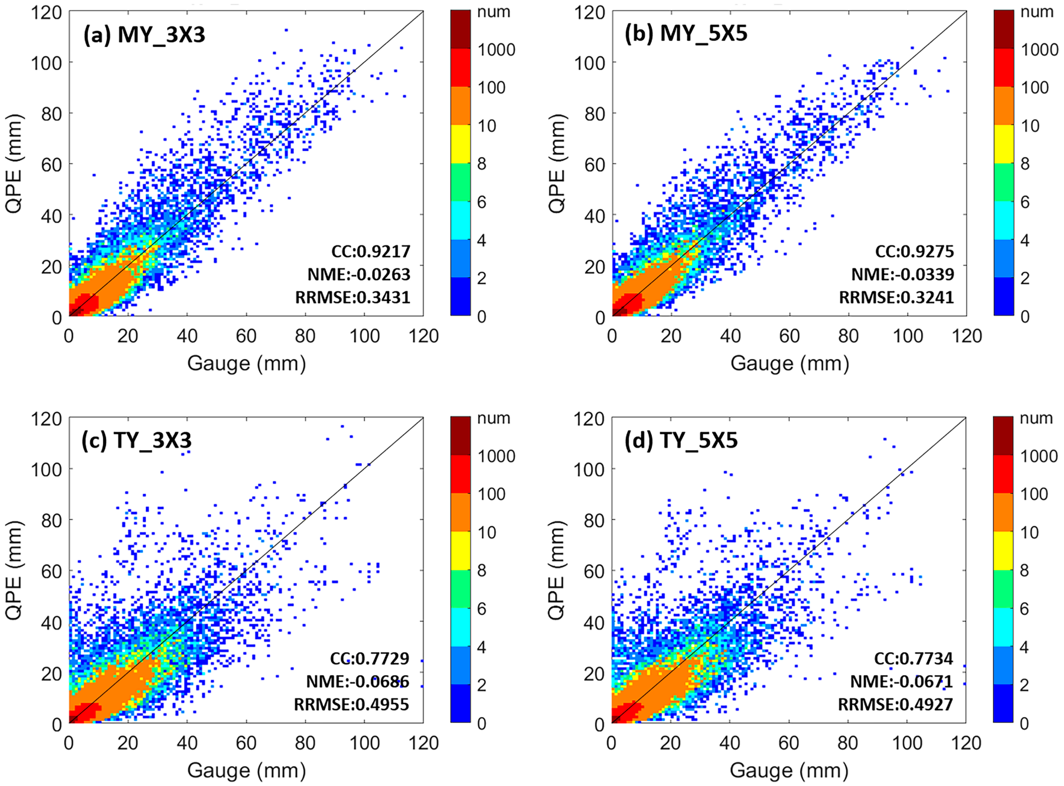

FIG. 15. Spatially averaged hourly SYNNT QPEs from (a),(b) mei-yu and (c),(d) typhoon events vs gauges. (a),(c) The 3 × 3 point-averaged QPEs. (b),(d) The 5 × 5 point averages. Detailed discussion can be found in the text.

Other factors that may have contributed to the larger QPE-gauge differences in typhoons than in the mei-yu events include 1) gauge undercatch and 2) large drifting effects of raindrops between the radar beam height and the surface; both would be enhanced in strong winds.

5. Summary

Effectively utilizing dual-polarization radar observations can enhance the performance of radar QPEs. The current study tries to improve the Taiwan operational radar QPE by developing localized radar–rain rate relationships using 3 years of disdrometer data from nine stations of an operational Parsivel network in northern Taiwan. The localized relationships included $R(Z)$, $R(A)$, and $R(K_{\mathrm{DP}})$. Further, a key parameter in $R(A)$ QPE, α, and its relationship to the Z_{DR}–Z slope, K, were investigated. The findings from our study are as follows:

1) The precipitation systems in northern Taiwan exhibited significant different drop size distributions than those in the United States with larger quantities of small rain droplets. The variation of DSDs highlights the need for the localizations of radar QPE schemes, particularly $R(Z)$ relationships. The QPE outcome of the DSD experiment demonstrated that the localized $R(Z)$ relationships led to a substantial reduction of NME from 1.08 to −0.03.
2) The DSD-based QPE experiment also showed that the $R(A)$ algorithm benefits significantly from the use of localized $\alpha(K)$ functions. These localized functions lead to an improvement of ∼13% in the NME over the nonlocalized version. The localized $R(A)$ coefficient, however, exhibited a less pronounced difference when compared to the current operational $R(A)$. Therefore, the operational $R(A)$ relationship with the local $\alpha(K)$ function performed comparably well to the localized $R(A)$ scheme.
3) The comparison of different radar–rain rate relationships revealed distinct features for each radar variable. Among them, the $R(A)$ scheme exhibits the highest correlation coefficient when compared to $R(Z)$ and $R(K_{\mathrm{DP}})$. Among the localized radar QPE relationships, $R(K_{\mathrm{DP}})$ reduced the RRMSE by 13.37% compared to $R(Z)$, and $R(A)$ provided an additional improvement of 9.73% with respect to $R(K_{\mathrm{DP}})$.
4) It was found that different radar variables provide different QPE accuracies for different rainfall intensities. In the QPE experiments based on DSD data, RZNT demonstrated the best performance in terms of RRMSE for rainfall intensities below 5 mm. RZOP significantly overestimated precipitation in light to moderate rain (i.e. 5–30 mm). In moderate to heavy rain (i.e., 10+ mm), $R(A)$ performed the best followed closely by $R(K_{\mathrm{DP}})$. These findings highlight the importance of combining different radar variables of Z, K_{DP}, and A into a synthetic QPE such that an optimal QPE can be obtained in a real-time operational system.

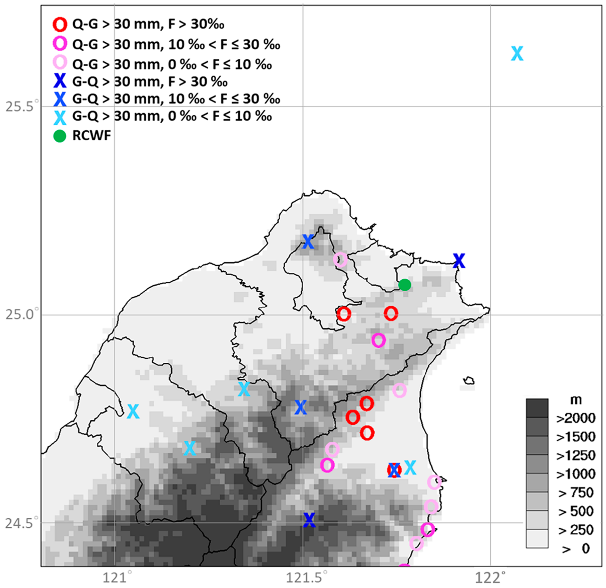

FIG. 16. The spatial distribution of the number frequency (F, ‰) of the hourly QPE-gauge differences exceeds 30 mm. The circles indicate the number frequency for QPE overestimation, and the X symbols indicate the QPE was underestimated. The green dot indicates the RCWF radar site. The gray shading represents the terrain height (m).

5) The QPE experiments with the RCWF weather radar showed that the localized synthetic QPE reduced the wet biases in the operational synthetic QPE for the relatively light rain (i.e., hourly rainfall $<$ 10–15 mm) for both the mei-yu and typhoon cases. This improvement is important since the wet biases in light rain have been a persistent issue in the Taiwan operational radar QPE. Further, the local synthetic QPE reduced the random errors in the typhoon QPE for hourly rainfalls below 50 mm. It is noted that the localized synthetic QPE had a ∼10% dry bias for hourly typhoon rainfalls of 15–60 mm where the operational synthetic QPE had little bias, indicating that additional factors need to be considered to further improve the localized QPE scheme.
6) A spatially relaxed QPE-gauge matching scheme was tested for the verification of the radar QPE and was found to effectively mitigate some uncertainties in the point-to-point radar QPE–gauge comparison. This experiment highlights the impact of radar and gauge sampling differences on the QPE verifications.
7) A significantly larger QPE uncertainties were found with the typhoons than with mei-yu events even with the spatial relaxed QPE–gauge matching scheme. This was likely related to an issue in the $R(A)$ QPE in the highly nonuniform blockage area that requires further refinements in the future.

In summary, the current study showed that the localized radar–rain rate relationships based on the DSD data in northern Taiwan provided improvements in the accuracy of operational QPEs. This study will be expanded island-wide to optimize the operational radar QPE algorithms for the C- and S-band weather radars in Taiwan.

Acknowledgments. The authors thank the Central Weather Administration for providing the radar data and computing resources. This work was supported by the Taiwan Water Resources Agency, the Agency of Rural Development and Soil and Water Conservation, and the Ministry of Science and Technology of Taiwan under Grants 111-2111-M-002-014, 111-2625-M-052-001, and 112-2625-M-052-001.

Data availability statement. The Parsivel, gauge, and radar data used in this study are from the Central Weather Administration. Owing to its proprietary nature, the supporting data cannot be openly shared. For details on accessing the data and the associated conditions, please refer to https://www.cwa.gov.tw/V8/E/S/service_guide.html.

REFERENCES

Barber, P. W., and S. C. Hill, 1990: *Light Scattering by Particles: Computational Methods*. World Scientific, 276 pp.

Brandes, E. A., G. Zhang, and J. Vivekanandan, 2002: Experiments in rainfall estimation with a polarimetric radar in a subtropical environment. *J. Appl. Meteor.*, **41**, 674–685, https://doi.org/10.1175/1520-0450(2002)041<0674:EIREWA>2.0.CO;2.

Bringi, V. N., and V. Chandrasekar, 2001: *Polarimetric Doppler Weather Radar: Principles and Applications*. Cambridge University Press, 636 pp., https://doi.org/10.1017/CBO9780511541094.

——, ——, N. Balakrishnan, and D. S. Zrnić, 1990: An examination of propagation effects in rainfall on radar measurements at microwave frequencies. *J. Atmos. Oceanic Technol.*, **7**, 829–840, https://doi.org/10.1175/1520-0426(1990)007<0829:AEOPEI>2.0.CO;2.

——, ——, J. Hubbert, E. Gorgucci, W. L. Randeu, and M. Schoenhuber, 2003: Raindrop size distribution in different climatic regimes from disdrometer and dual-polarized radar analysis. *J. Atmos. Sci.*, **60**, 354–365, https://doi.org/10.1175/1520-0469(2003)060<0354:RSDIDC>2.0.CO;2.

Chang, P.-L., and Coauthors, 2021: An operational multi-radar multi-sensor QPE system in Taiwan. *Bull. Amer. Meteor. Soc.*, **102**, E555–E577, https://doi.org/10.1175/BAMS-D-20-0043.1.

Chang, W.-Y., T.-C. C. Wang, and P.-L. Lin, 2009: Characteristics of the raindrop size distribution and drop shape relation in typhoon systems in the western Pacific from the 2D video disdrometer and NCU C-band polarimetric radar. *J. Atmos. Oceanic Technol.*, **26**, 1973–1993, https://doi.org/10.1175/2009JTECHA1236.1.

Chen, C.-S., and Y.-L. Chen, 2003: The rainfall characteristics of Taiwan. *Mon. Wea. Rev.*, **131**, 1323–1341, https://doi.org/10.1175/1520-0493(2003)131<1323:TRCOT>2.0.CO;2.

Chen, G. T.-J., 1992: Mesoscale features observed in the Taiwan mei-yu season. *J. Meteor. Soc. Japan*, **70**, 497–516, https://doi.org/10.2151/jmsj1965.70.1B_497.

——, 2004: Research on the phenomena of meiyu during the past quarter century: An overview. *East Asian Monsoon*, C.-P. Chang, Ed., World Scientific, 357–403.

Chen, J.-Y., W.-Y. Chang, and P.-L. Chang, 2021: A synthetic quantitative precipitation estimation by integrating S- and C-band dual-polarization radars over northern Taiwan. *Remote Sens.*, **13**, 154, https://doi.org/10.3390/rs13010154.

Chen, Y.-L., 1993: Some synoptic-scale aspects of the surface fronts over southern China during TAMEX. *Mon. Wea. Rev.*, **121**, 50–64, https://doi.org/10.1175/1520-0493(1993)121<0050:SSSAOT>2.0.CO;2.

Cifelli, R., V. Chandrasekar, S. Lim, P. C. Kennedy, Y. Wang, and S. A. Rutledge, 2011: A new dual-polarization radar rainfall algorithm: Application in Colorado precipitation events. *J. Atmos. Oceanic Technol.*, **28**, 352–364, https://doi.org/10.1175/2010JTECHA1488.1.

Cocks, S. B., and Coauthors, 2019: A prototype quantitative precipitation estimation algorithm for operational S-band polarimetric radar utilizing specific attenuation and specific differential phase. Part II: Performance verification and case study analysis. *J. Hydrometeor.*, **20**, 999–1014, https://doi.org/10.1175/JHM-D-18-0070.1.

Friedrich, K., E. A. Kalina, F. J. Masters, and C. R. Lopez, 2013a: Drop-size distributions in thunderstorms measured by optical disdrometers during VORTEX2. *Mon. Wea. Rev.*, **141**, 1182–1203, https://doi.org/10.1175/MWR-D-12-00116.1.

——, S. Higgins, F. J. Masters, and C. R. Lopez, 2013b: Articulating and stationary PARSIVEL disdrometer measurements in conditions with strong winds and heavy rainfall. *J. Atmos. Oceanic Technol.*, **30**, 2063–2080, https://doi.org/10.1175/JTECH-D-12-00254.1.

Fulton, R. A., J. P. Breidenbach, D.-J. Seo, D. A. Miller, and T. O'Bannon, 1998: The WSR-88D rainfall algorithm. *Wea. Forecasting*, **13**, 377–395, https://doi.org/10.1175/1520-0434(1998)013<0377:TWRA>2.0.CO;2.

Kao, Y.-C., and P.-F. Lin, 2023: Technological development of rain gauge data verification in Taiwan area (in Chinese). *Proc. Conf. Weather Analysis and Forecasting*, Taipei, Taiwan, Central Weather Bureau.

Kumjian, M. R., 2013: Principles and applications of dual-polarization radar. Part I: Description of the polarimetric radar variables. *J. Oper. Meteor.*, **1**, 226–242, https://doi.org/10.15191/nwajom.2013.0119.

Lee, M.-T., P.-L. Lin, W.-Y. Chang, B. K. Seela, and J. Janapati, 2019: Microphysical characteristics and types of precipitation for different seasons over North Taiwan. *J. Meteor. Soc. Japan*, **97**, 841–865, https://doi.org/10.2151/jmsj.2019-048.

Li, H., D. Moisseev, Y. Luo, L. Liu, Z. Ruan, L. Cui, and X. Bao, 2023: Assessing specific differential phase (K_{DP})-based quantitative precipitation estimation for the record-breaking rainfall over Zhengzhou city on 20 July 2021. *Hydrol. Earth Syst. Sci.*, **27**, 1033–1046, https://doi.org/10.5194/hess-27-1033-2023.

Loh, J. L., W.-Y. Chang, H.-W. Hsu, P.-F. Lin, P.-L. Chang, Y.-L. Teng, and Y.-C. Liou, 2022: Long-term assessment of the reflectivity biases and wet-radome effect using collocated operational S- and C-band dual-polarization radars. *IEEE Trans. Geosci. Remote Sens.*, **60**, 5113217, https://doi.org/10.1109/TGRS.2022.3170609.

Lu, K.-X., Y.-S. Tang, P.-F. Lin, T.-C. Chen, and P.-L. Chang, 2020: Quality control and analyses of the disdrometer network in Taiwan. *Atmos. Sci.*, **48**, 44–92.

Marshall, J. S., W. Hitschfeld, and K. L. S. Gunn, 1955: Advances in radar weather. *Advances in Geophysics*, Vol. 2, Academic Press, 1–56, https://doi.org/10.1016/S0065-2687(08)60310-6.

Miller, M. A., J. Verlinde, C. V. Gilbert, G. J. Lehenbauer, J. S. Tongue, and E. E. Clothiaux, 1998: Detection of nonprecipitating clouds with the WSR-88D: A theoretical and experimental survey of capabilities and limitations. *Wea. Forecasting*, **13**, 1046–1062, https://doi.org/10.1175/1520-0434(1998)013<1046:DONCWT>2.0.CO;2.

Ryzhkov, A. V., and D. Zrnić, 2005: Radar polarimetry at S, C, and X bands: Comparative analysis and operational implications. *32nd Int. Conf. on Radar Meteorology*, Albuquerque, NM, Amer. Meteor. Soc., 9R.3, https://ams.confex.com/ams/32Rad11Meso/techprogram/paper_95684.htm.

——, M. Diederich, P. Zhang, and C. Simmer, 2014: Potential utilization of specific attenuation for rainfall estimation, mitigation of partial beam blockage, and radar networking. *J. Atmos. Oceanic Technol.*, **31**, 599–619, https://doi.org/10.1175/JTECH-D-13-00038.1.

——, P. Zhang, P. Bukovčić, J. Zhang, and S. Cocks, 2022: Polarimetric radar quantitative precipitation estimation. *Remote Sens.*, **14**, 1695, https://doi.org/10.3390/rs14071695.

Seliga, T. A., V. N. Bringi, and H. H. Al-Khatib, 1981: A preliminary study of comparative measurements of rainfall rate using the differential reflectivity radar technique and a raingauge network. *J. Appl. Meteor.*, **20**, 1362–1368, https://doi.org/10.1175/1520-0450(1981)020<1362:APSOCM>2.0.CO;2.

Smith, J. A., M. L. Baeck, Y. Su, M. Liu, and G. A. Vecchi, 2023: Strange storms: Rainfall extremes from the remnants of Hurricane Ida (2021) in the northeastern US. *Water Resour. Res.*, **59**, e2022WR033934, https://doi.org/10.1029/2022WR033934.

Steiner, M., R. A. Houze Jr., and S. E. Yuter, 1995: Climatological characterization of three-dimensional storm structure from operational radar and rain gauge data. *J. Appl. Meteor.*, **34**, 1978–2007, https://doi.org/10.1175/1520-0450(1995)034<1978:CCOTDS>2.0.CO;2.

Tang, L., J. Zhang, C. Langston, J. Krause, K. Howard, and V. Lakshmanan, 2014: A physically based precipitation–nonprecipitation radar echo classifier using polarimetric and environmental data in a real-time national system. *Wea. Forecasting*, **29**, 1106–1119, https://doi.org/10.1175/WAF-D-13-00072.1.

Testud, J., E. Le Bouar, E. Obligis, and M. Ali-Mehenni, 2000: The rain profiling algorithm applied to polarimetric weather radar. *J. Atmos. Oceanic Technol.*, **17**, 332–356, https://doi.org/10.1175/1520-0426(2000)017<0332:TRPAAT>2.0.CO;2.

Ulbrich, C. W., and D. Atlas, 1984: Assessment of the contribution of differential polarization to improved rainfall measurements. *Radio Sci.*, **19**, 49–57, https://doi.org/10.1029/RS019i001p00049.

Wang, Y., P. Zhang, A. V. Ryzhkov, J. Zhang, and P.-L. Chang, 2014: Utilization of specific attenuation for tropical rainfall estimation in complex terrain. *J. Hydrometeor.*, **15**, 2250–2266, https://doi.org/10.1175/JHM-D-14-0003.1.

——, J. Zhang, P. Zhang, A. V. Ryzhkov, and C. Fritts, 2017: The impact of different precipitation types on the polarimetric radar QPE using specific attenuation. *38th Int. Conf. on Radar Meteorology*, Chicago, IL, Amer. Meteor. Soc., 265, https://ams.confex.com/ams/38RADAR/webprogram/Paper321106.html.

——, S. Cocks, L. Tang, P. Zhang, A. Ryzhkov, J. Zhang, and K. Howard, 2019: A prototype quantitative precipitation estimation algorithm for operational S-band polarimetric radar utilizing specific attenuation and specific differential phase. Part I: Algorithm description. *J. Hydrometeor.*, **20**, 985–997, https://doi.org/10.1175/JHM-D-18-0071.1.

Waterman, P. C., 1971: Symmetry, unitarity and geometry in electromagnetic scattering. *Phys. Rev.*, **3D**, 825–839, https://doi.org/10.1103/PhysRevD.3.825.

Xie, Y., S. E. Koch, J. A. McGinley, S. Albers, and N. Wang, 2005: A sequential variational analysis approach for mesoscale data assimilation. *21th Conf. on Weather Analysis and Forecasting/17th Conf. on Numerical Weather Prediction*. Washington, DC, Amer. Meteor. Soc., 15B.7, https://ams.confex.com/ams/WAFNWP34BC/techprogram/paper_93468.htm.

——, S. Koch, J. McGinley, S. Albers, P. E. Beringer, M. Wolfson, and M. Chan, 2011: A space–time multiscale analysis system: A sequential variational analysis approach. *Mon. Wea. Rev.*, **139**, 1224–1240, https://doi.org/10.1175/2010MWR3338.1.

Xin, L., G. Recuter, and B. Larochelle, 1997: Reflectivity-rain rate relationships for convective rainshowers in Edmonton: Research note. *Atmos.–Ocean*, **35**, 513–521, https://doi.org/10.1080/07055900.1997.9649602.

You, C.-H., M.-Y. Kang, D.-I. Lee, and H. Uyeda, 2014: Rainfall estimation by S-band polarimetric radar in Korea. Part I: Preprocessing and preliminary results. *Meteor. Appl.*, **21**, 975–983, https://doi.org/10.1002/met.1454.

Zhang, J., L. Tang, S. Cocks, P. Zhang, A. Ryzhkov, K. Howard, C. Langston, and B. Kaney, 2020: A dual-polarization radar synthetic QPE for operations. *J. Hydrometeor.*, **21**, 2507–2521, https://doi.org/10.1175/JHM-D-19-0194.1.

Zhang, L., J. Min, X. Zhuang, and R. S. Schumacher, 2019: General features of extreme rainfall events produced by MCSs over East China during 2016–17. *Mon. Wea. Rev.*, **147**, 2693–2714, https://doi.org/10.1175/MWR-D-18-0455.1.

Zheng, A.-R., R.-H. Lee, X.-Y. Gu, H.-X. Gao, and Y.-W. Chen, 2011: Gauge data quality control in the real-time system (in Chinese). *Proc. Conf. Weather Analysis and Forecasting*, Taipei, Taiwan, Central Weather Bureau, https://photino.cwb.gov.tw/rdcweb/lib/cd/cd01conf/100doc/46.pdf.

Zrnić, D. S., and A. V. Ryzhkov, 1999: Polarimetry for weather surveillance radars. *Bull. Amer. Meteor. Soc.*, **80**, 389–406, https://doi.org/10.1175/1520-0477(1999)080<0389:PFWSR>2.0.CO;2.

——, V. M. Melnikov, and J. K. Carter, 2006: Calibrating differential reflectivity on the WSR-88D. *J. Atmos. Oceanic Technol.*, **23**, 944–951, https://doi.org/10.1175/JTECH1893.1.